Design of a High-Dynamic-Range Prototype Readout System for VLAST Calorimeter*

Qiang Wan,[1,2] Jian-Hua Guo,[1,2,†] Xing Xu,[1,2] Shen Wang,[1] Yong-Qiang Zhang,[1] Yi-Ming Hu,[1] Yan Zhang,[1] Xu Pan,[1,2] Xiang Li,[1] Chuan Yue,[1] Wei Jiang,[1] Yu-Xin Cui,[1,2] and Deng-Yi Chen[1]

[1]*Key Laboratory of Dark Matter and Space Astronomy, Purple Mountain Observatory, Chinese Academy of Sciences, Nanjing 210023, China*

[2]*School of Astronomy and Space Science, University of Science and Technology of China, Hefei 230026, China*

In the future, the Very Large Area gamma-ray Space Telescope (VLAST) is expected to observe high-energy electrons and gamma rays in the MeV to TeV range with unprecedented acceptance. As part of the detector suite, a high-energy imaging calorimeter (HEIC) is currently being developed as a homogeneous calorimeter that utilizes long bismuth germanate (BGO) scintillation crystals as both absorbers and detectors. To accurately measure the energy deposition in the BGO bar of HEIC, a high-dynamic-range readout method using a silicon photoMultiplier (SiPM) and multiphotodiode (PD) with different active areas has been proposed. A prototype readout system that adopts multichannel charge measurement ASICs was also developed to read out the combined system of SiPMs and PDs. Preliminary tests confirmed the feasibility of the readout scheme, which is expected to have a dynamic range close to 10^6.

Keywords: VLAST, Calorimeter, Readout system, Front-end electronics, Large dynamic range

I. INTRODUCTION

The Fermi Large Area Telescope (Fermi-LAT) has been in orbit for more than a decade and is considered the most successful gamma-ray space-based detector to date [1]. The All-sky Medium Energy Gamma-ray Observatory eXplorer (AMEGO-X) is being planned as a successor to Fermi-LAT, with a primary focus on operating in the MeV energy band [2]. Another space-based gamma-ray telescope being developed is GAMMA-400 by Russia. Its main feature is unprecedented angular resolution at energies greater than 30 GeV [3].

In China, the DArk Matter Particle Explorer (DAMPE) has made significant progress in the direct detection of cosmic and gammarays since its successful launch in 2015 [4–9]. However, its detector size limits the acceptance of gamma rays. The High Energy cosmic-Radiation Detection Facility (HERD) is a large space mission under preparation that is scheduled for installation on the Chinese Space Station (CSS) in 2027 [10]. HERD will significantly improve the ability to detect high-energy cosmic rays [11]; however, its low Earth orbit also limits gamma-ray observations.

Gamma-ray detection is vital for studying dark matter, astrophysics, and cosmic rays [12–14]. Therefore, the Very Large Area gamma-ray Space Telescope (VLAST) was proposed by scientists from the DAMPE collaboration to develop a world-leading detector for gamma rays. Compared with other space-based detectors, the effective acceptance of VLAST is significantly higher, which makes it more sensitive to gamma photons and more precise in its measurements [15].

Fig. 1 illustrates the initial design of the VLAST detector, comprising three subdetectors: an anti-coincidence detector (ACD), a silicon Tracker, a low-energy gamma-ray detector (STED), and a high-energy imaging calorimeter (HEIC). The ACD is composed of organic plastic scintillator tiles to distinguish charged particles from gamma photons and identify nuclides in cosmic rays [16]. The STED features a multilayer structure consisting of double-sided silicon microstrip detectors [17] and alternating cesium iodide (CsI) crystals, which scatter low-energy gamma photons while converting high-energy photons into positron-electron pairs. The HEIC accurately measures the energy of electrons and photons and images the shape of the electromagnetic cascade shower in the calorimeter. The VLAST design combines the advantages of DAMPE [18] and APT [19]. Its most significant innovation lies in the utilization of CsI crystals instead of traditional tungsten plates in the silicon tracker. This enables the measurement of MeV photons using the Compton effect and effectively improves the energy resolution of gamma rays below the GeV range. In combination with the calorimeter, the entire VLAST detector extends the detection range of gamma rays from MeV to TeV, substantially improving observation sensitivity and accuracy.

The HEIC is a large area detector composed of 2×2 calorimeter modules, each of which is composed of eight layers of long BGO crystals stacked orthogonally, with a planned crystal size of $120\,\mathrm{cm} \times 2.5\,\mathrm{cm} \times 2.5\,\mathrm{cm}$. The calorimeter measures the energy range of photons and electrons from $0.1\,\mathrm{GeV}$ to $20\,\mathrm{TeV}$, depending on the scientific requirements. When photons or electrons hit the detector, they deposit energy in the crystal units via an electromagnetic cascade shower. The calorimeter must accurately measure the spatial distribution of the shower to select high-energy photons and exclude protons from cosmic rays. Based on simulations, each crystal detector unit must read a minimum signal of $0.1 \sim 0.2$ MIPs for the energy deposition, which can also generate the corresponding trigger decision signal. The maximum energy deposition of BGO crystals located at the center of the shower for photons and electrons with a maximum energy of 20 TeV is approximately 2×10^5 MIPs, where MIP represents the energy deposition by a minimum ioniza-

* Supported by the National Natural Science Foundation of China (Nos. 12227805, U1831206, 12103095, 12235012, 12273120, 11973097) and the Scientific Instrument Developing Project of the Chinese Academy of Sciences (No. GJJSTD20210009)

† Corresponding author, jhguo@pmo.ac.cn

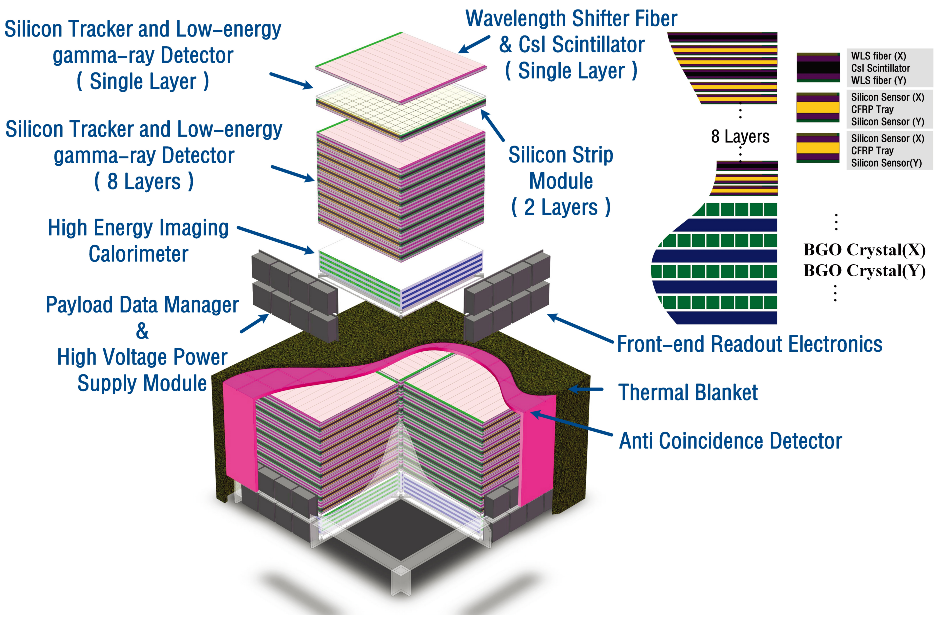

Fig. 1. Architecture of the VLAST

tion particle (MIP) through a BGO crystal of $2.5\,\mathrm{cm}$ thickness, which is approximately $22.5\,\mathrm{MeV}$.

In conclusion, achieving an extremely wide dynamic range of at least six orders of magnitude is the primary challenge in designing a VLAST calorimeter readout system. This paper proposes a readout scheme that utilizes a combination of a silicon photomultiplier (SiPM) and multiphotodiode (PD) to achieve high energy resolution and a large dynamic range. Furthermore, a small calorimeter module was developed, and a corresponding readout prototype system was designed to serve as a technical reference for future studies on the VLAST calorimeter.

II. HIGH-DYNAMIC-RANGE READOUT METHOD

The readout of a calorimeter typically involves two components: photodetectors and readout electronics. However, the dynamic range of a single readout device and measurement channel can be limited by various issues, such as interference, noise, and saturation. To overcome these limitations, many international studies have used photodetectors or readout electronics with different gains to extend the dynamic range.

The calorimeters of Fermi-LAT [20], CALET-CAL [21] and HERD [22] adopt readout methods that involve either PD with PD or PD with avalanche photodiode (APD) combination systems. PDs with different sensitive areas or APDs with different gains are responsible for different energy ranges. For the same readout electronic channel, PDs with larger sensitive areas and APDs with higher gains are used to measure signals in the low-energy range, whereas PDs with smaller sensitive areas are used to measure signals in the high-energy range. Each of their readout electronics is also equipped with two different gain readout channels to further expand the dynamic range.

The readout method of the BGO calorimeter of DAMPE utilizes identical electronic measurement channels connected to three different dynodes of one photomultiplier tube (PMT). Three channels with different gains are responsible for detecting signals in different energy ranges, allowing for a larger dynamic range of measurements [23].

There are a few issues with the PMT multidynode readout scheme in terms of the design and requirements of the VLAST calorimeter. First, the resistance network between the PMT dynodes results in a longer recovery time for large signals. This can cause an accumulation of low-energy and high-flux signals, which can be problematic for large area detectors. Simultaneously, crosstalk occurs between the signals from different dynodes of one PMT. Second, PMT generally has a large volume and causes a relatively large dead zone when combined to form a large area detector for the VLAST calorimeter. It requires high voltage to operate and is sensitive to magnetic field.

Compared to PMT, semiconductor photodetectors offer several advantages, including smaller size, immunity to magnetic fields, and lower bias voltage. Consequently, they are highly suitable for the scintillation of the VLAST calorimeter. To ensure the required measurement range of the the VLAST calorimeter, using only PDs without gain requires an exceptionally low noise level in electronics for small signals. However, if an APD with a higher gain is employed to measure small signals, the output current of the APD will continuously increase as the measured light signal increases. This can potentially interfere with other channels even if the electronics are already saturated. Therefore, using SiPM is the most suit-

able option for measuring small signals because the saturation range of SiPM is solely determined by the number of pixels.

The preliminary readout scheme for VLAST calorimeter is shown in Fig. 2. A SiPM and a pair of PDs with different sensitive areas were selected to form a crystal detector unit coupled with a BGO bar end face. The SiPM is Hamamatsu S14160-3010PS with an effective photosensitive area of $3 \times 3\,\mathrm{mm}^2$, 89984 pixels, and a typical gain of 1.8×10^5. The large PD (L-PD) is Hamamatsu S2744-08 with a sensitive area of $10 \times 20\,\mathrm{mm}^2$, whereas the small PD (S-PD) is Hamamatsu S8729-10 with a sensitive area of $2 \times 3.3\,\mathrm{mm}^2$. The overall measurement range was divided into three sections. The SiPM with the highest gain was used to detect the lowest energy signals, whereas two PDs of different sizes were used to detect signals in the middle and highest energy ranges, respectively. Using the relative gain between the three detectors, the dynamic range can be expanded.

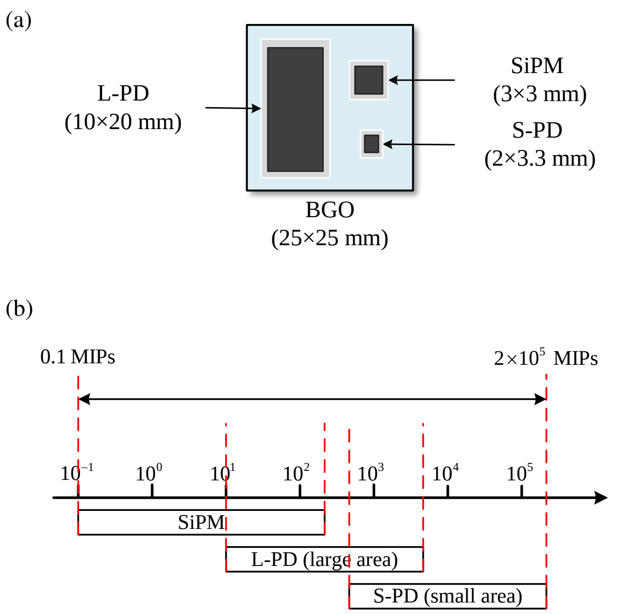

Fig. 2. Readout scheme of VLAST calorimeter. (a) Diagram of the detector unit. (b) Design concept of a large dynamic range.

Owing to the nonlinearity of SiPM, only a fraction of the pixels ranging from one-third to half was utilized. The light yield of the BGO crystals was estimated to be approximately $8000\,\mathrm{photons/MeV}$ [24, 25], resulting in a maximum measurable energy greater than $100\,\mathrm{MIPs}$ for SiPMs. This corresponds to an output charge of approximately $800\,\mathrm{pC}$. The sensitive area ratio between the two PDs was 30, and their output charge ratio was also 30. When using the same electronic channel for readout, the gain in the middle- and high-energy ranges is also 30, and the corresponding output charges are approximately in the range of tens of fC to $15\,\mathrm{pC}$.

III. ARCHITECTURE OF THE PROTOTYPE READOUT SYSTEM

Typically, the number of readout channels for imaging calorimeters is extremely high. However, both the space and power resources are strictly limited in space experiments. Therefore, utilizing multichannel ASICs to design the readout electronics is the only viable option. Considering the dynamic range of the three photodetectors and the light decay time of the BGO crystal (approximately $300\,\mathrm{ns}$), three commercial ASICs (i.e., IDE3380, VATA160, and VA160) developed by IDEAS Inc. in Norway [26] were chosen for the readout of SiPM, L-PD, and S-PD, respectively. Notably, VATA160 and VA160 were already successfully implemented in the DAMPE BGO calorimeter. By utilizing these three ASICs, a readout electronics system was designed to verify the feasibility of the multiphotodetector readout scheme and the performance of the SiPM and PD combined system.

The structure of the prototype readout system is illustrated in Fig. 3, which mainly consists of front-end electronics (FEE) and a data acquisition (DAQ) system. The DAQ system includes a DAQ module and DAQ software. The FEE is responsible for analog integration, filtering and shaping, and digitization of the signals from SiPM and PD. It also packages and transfers the acquired data to the DAQ system. The DAQ module can connect to four FEE boards, which are responsible for sending commands to all FEEs and collecting and transmitting the data acquired by all FEEs. In addition, it integrates trigger logic. Based on the hit signals from the FEEs, the trigger system generates trigger signals through a logical decision to control the data acquisition process of the FEEs. The DAQ software runs on a computer, providing a visualization operation program for controlling the entire system and processing and storing the acquired data. Fig. 4 shows a photograph of the FEE board and DAQ module.

IV. DESIGN OF THE FEE

The first version of the prototype readout system for the VLAST calorimeter uses one IDE3380, one VATA160, and one VA160 on each FEE board, which can connect 16 detection units. The bias voltage of the photodetector is sourced from a low-noise power supply (Keysight B1962A) and filtered through the circuitry of the FEE. Unlike SiPM, the bias voltage of PD usually remains constant during operation. Given that the L-PD and S-PD require differing bias voltages, a low dropout regulator (LDO) was incorporated into the FEE design to provide a bias voltage specifically for them.

Additionally, there are calibration circuits on the FEE used for calibrating ASICs and circuits for monitoring ASIC power current and ambient temperature. The logic circuits in the FPGA were designed to control these circuits and process data.

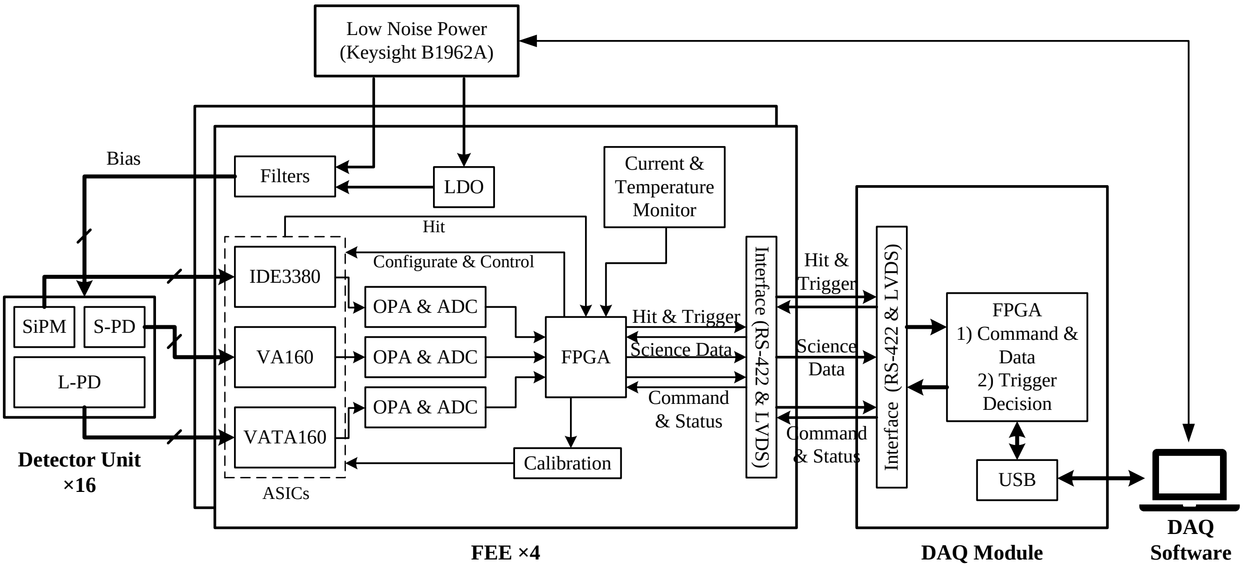

Fig. 3. Block diagram of the prototype readout system

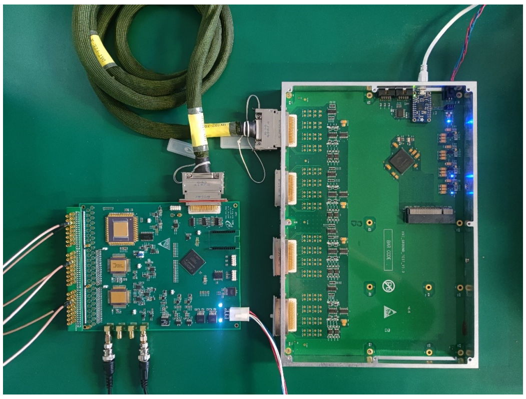

Fig. 4. Photo of an FEE and DAQ module

A. Charge measurement ASIC

The IDE3380 features a programmable dynamic range that can be adjusted to suit photodetectors with high gain, such as PMT and SiPM. The shaping times can also be set programmatically to match different scintillators. Fig. 5 shows a schematic of the IDE3380 chip.

The IDE3380 consists of 16 identical analog readout channels and a summation channel, which is used to sum 16 input signals and primarily serves as a readout for multichannel detector arrays. Each analog readout channel comprises two circuits: slow and fast shaping. The slow-shaping circuit integrates the analog current pulse from the detector to measure its charge, whereas the fast-shaping circuit utilizes a threshold comparator to screen over-threshold signals and generate a trigger signal [27].

Furthermore, the IDE3380 is equipped with a current-mode input stage (CMIS) on the input end of each channel. The CMIS is designed to handle larger input signals through adjustable attenuation multiples while also improving the input impedance of the electronics channel. This allows the channel to accommodate detectors with high capacitive loads and leakage currents. The CMIS also includes an adjustable bias current source that compensates for the leakage current of the detector and a bias voltage source that fine-tunes the detector‘s bias voltage to adjust its gain. In the presence of CMIS, the DC coupling connection mode between SiPM and IDE3380 is more suitable.

The structure and function of VATA160 closely resemble those of IDE3380. As illustrated in Fig. 6, VATA160 consists of two distinct components: the VA and TA parts. The left VA performs charge measurements, whereas the right TA generates trigger signals. The structure of VA160 is identical to that of the VA of VATA160. However, the VATA160 / VA160 has a fixed dynamic range and shaping time, which distinguishes it from IDE3380. They are also not equipped with CMIS; thus, L-PD and S-PD are connected to VATA160 and VA160, respectively, by AC coupling.

B. Calibration circuit

Fig. 7 shows a schematic diagram of the calibration circuit. The digital-to-analog converter (DAC) and operational amplifier (OPA) provide DC voltage. The single-pole double-throw analog switch switches from R1 to R2 under the control of FPGA logic and generates a step voltage in the circuit. The amplitude of the step voltage is determined by the difference between the DC and power supply voltages and can

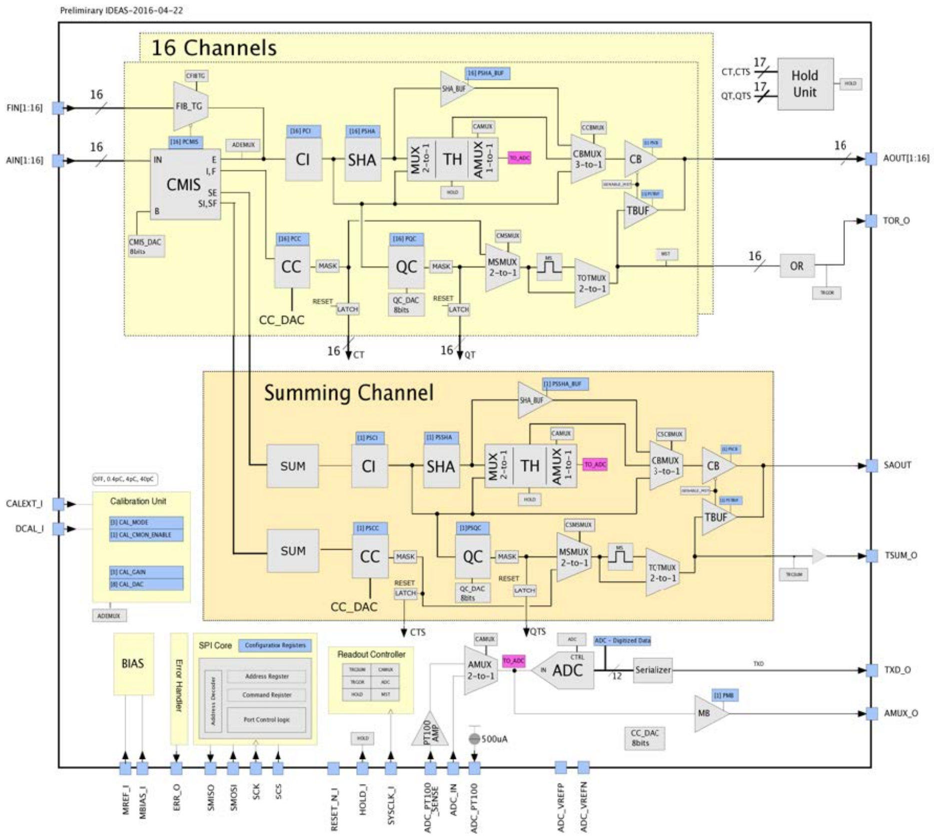

Fig. 5. Schematic diagram of IDE3380

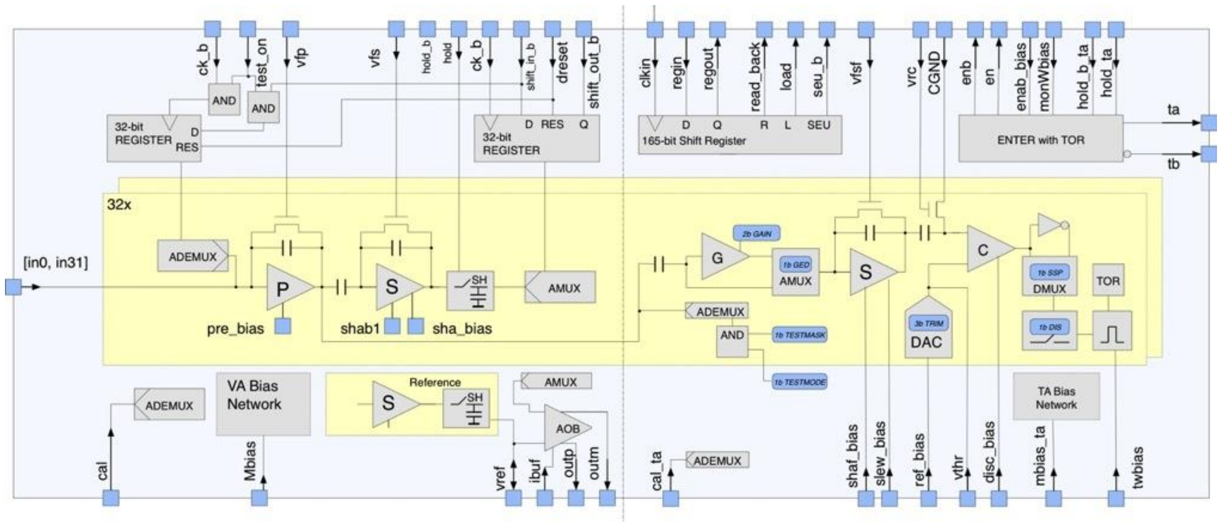

Fig. 6. Schematic diagram of VATA160

be set by adjusting the DAC. The step voltage generates current pulses that are injected into the calibration module of the charge measurement ASICs using high-precision capacitors. The charge of the current pulse is determined by the product of the step voltage amplitude and capacitance. An analog multiplexer inside both IDE3380 and VATA160 is designed to select the calibration channels. By controlling the multiplexer to select each channel sequentially and scanning it to adjust the DAC, calibration pulse signals with different charges can be generated, and each channel can be calibrated accordingly.

The calibration circuit uses the method of switching the analog switch from the operational amplifier to the positive

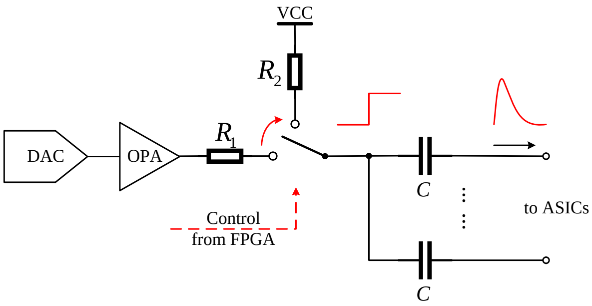

Fig. 7. Block diagram of the calibration circuit

power supply to generate calibration charge pulses. With this design, the operational amplifier does not require a large bandwidth and slew rate to generate a current pulse signal with a fast-rising edge, which can be as close as possible to the time characteristics of the detector output signal. In the process of switching the analog switch back and forth, the charge and discharge speeds of capacitor C are determined by R1 and R2, respectively.

C. Current and temperature monitoring circuit

Fig. 8 shows a schematic of the ASIC power-current monitoring circuit [28]. A separate LDO was used to supply power to the charge measurement chip. A sampling resistor is connected in series to the ASIC power supply to measure the voltage difference across it, which allows the monitoring of the working current of the ASIC. The voltage across the sampling resistor is collected using an integrated instrumentation amplifier and an analog-to-digital converter (ADC). The instrumentation amplifier has a high input impedance and common-mode rejection ratio, minimizing the load and interference of the measurement circuit on the ASIC power supply current. In addition, it can measure even the slightest changes in the current with high accuracy. The FPGA logic runs a comparison algorithm that determines the working status of the charge measurement chip by comparing the value collected by the current monitoring with the preset threshold and subsequently takes corresponding measures.

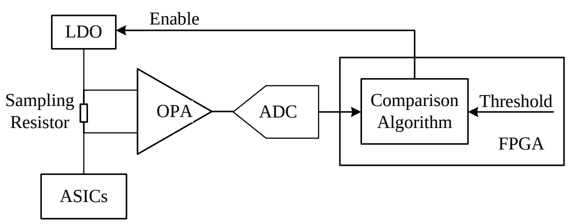

Fig. 8. Block diagram of the current monitoring circuit

The performance of semiconductor detectors can be easily affected by environmental temperature; therefore, it is necessary to monitor the working environment temperature. A high-precision digital temperature sensor, ADT7320, was used directly on the FEE board to measure the temperature. Its operating temperature range is $-40 \sim 150\,^{\circ}\mathrm{C}$, and the 16-bit precision enables a temperature resolution of up to $0.0078\,^{\circ}\mathrm{C}$. Simultaneously, ADT7320 can also generate an interrupt signal when the temperature exceeds the preset range, and its function and threshold can be programmed and configured.

D. Control logic in FPGA

The main function block diagram of FPGA logic is shown in Fig. 9. The FPGA logic circuit is primarily responsible for managing the data transmission process. When triggered, it sequentially collects, packs, and verifies the charge measurement data from all channels, along with trigger information and other relevant data. The compiled scientific data are stored in the cache and transmitted to the DAQ system in synchronous serial mode via the LVDS interface.

In addition to performing high-precision charge measurements, another important function of the FEE is providing hit information to indicate whether the corresponding detection unit has been hit. The minimum trigger condition for the calorimeter is based on the hit state of a layer rather than a single crystal [29]. The raw hit signals from IDE3380 and VATA160 are generated through the logical "OR" of all channels. By configuring the registers of ASIC, only the channels corresponding to a certain layer can be selected to generate hit signals. The hit and trigger processors in the FPGA process the raw hit signals from the ASIC, generate hit signals, and send them to the trigger system of the DAQ module. The trigger system generates trigger signals through logical decision and sends them back to the FEE to control the scientific data acquisition process. The hit and trigger signals are transmitted between the FEE and the DAQ module through two RS-422 simplex interfaces.

The DAQ system also sends commands to FEEs to perform tasks such as configuring the ASIC and controlling the calibration circuits. In response to the DAQ's commands, the FEE sends operational status information, such as current and temperature data, to the DAQ for processing. To enable communication between the FEE and DAQ modules, an RS-422 half-duplex interface was used to transmit both the commands and state data.

V. PERFORMANCE OF THE PROTOTYPE SYSTEM

The VLAST calorimeter aims to create a large area detector using BGO bars with a length of 1.2 meters. Currently, the crystals are being prepared on a meter scale. However, for the purposes of this study, a calorimeter module was constructed using smaller BGO crystals with dimensions of $25\,\mathrm{mm} \times 25\,\mathrm{mm} \times 600\,\mathrm{mm}$. It comprises 15 BGO bars arranged in six layers orthogonal to each other, with two or

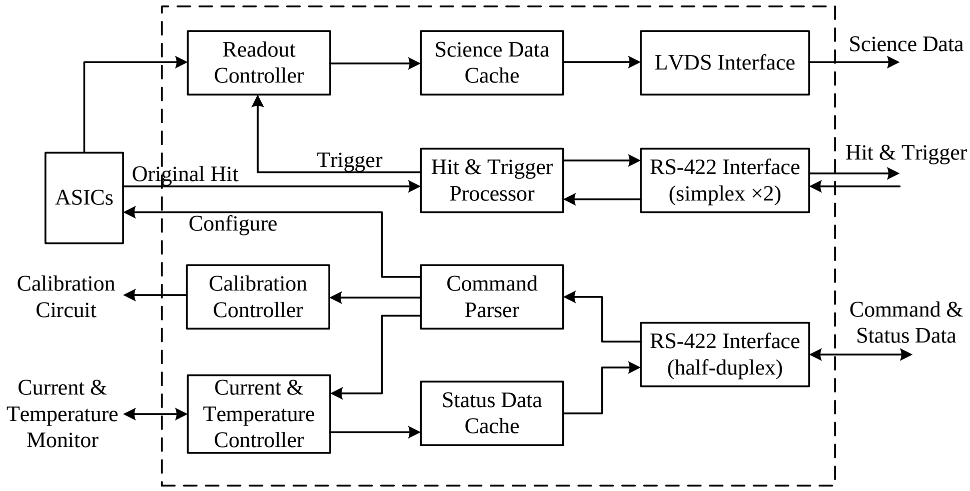

Fig. 9. Functional block diagram of FPGA logic

three crystals per layer. A photodetector unit is installed at one end of each bar. Two FEE boards are responsible for reading all the detector units on the two sides of the calorimeter module, with each FEE board connected to seven or eight detector units. A series of tests was conducted to evaluate the function and performance of the prototype readout system.

A. Baseline noise

The equivalent input capacitance of the preamplifier is increased owing to the junction capacitance of the semiconductor detector and the distributed capacitance of the signal cable. This increase in capacitance affects the noise level of the electronics system. Moreover, the signal cable between the detector and electronics may introduce electromagnetic interference. To evaluate the effect of the cable connection on the noise in the measurement circuit, we employed two methods, that is, using either single-core wires or coaxial cables to connect the photodetector to FEE. The outer layer of the coaxial cable connects the electronic ground with the mechanical ground of the detector module structure. The baseline noise of the eight channels connected to the detector on one FEE board was tested, and the results are shown in Fig. 10.

Because of the CMIS at the input end of IDE3380, it can effectively reduce the effect of the equivalent input capacitance on the noise of the charge-sensitive amplifier. Consequently, the baseline noise of each channel of IDE3380 does not significantly increase after connecting the SiPM. Moreover, no significant differences were observed when using either single-core wires or coaxial cables for the connection.

However, both VATA160 and VA160 exhibit an increase in channel noise upon connecting to L-PD and S-PD, respectively. At this point, using coaxial cable has a certain effect on shielding interference compared to a single-core wire connection. Moreover, their noise levels are essentially the same under the same connection configuration.

B. Electronic linearity

By using a signal source to generate a step pulse, a current pulse can be generated and injected into the electronic channel through a series-connected capacitor. The charge of the current pulse is determined by multiplying the amplitude of the step voltage by the capacitor value. To calibrate the linearity of the electronic channel, the amplitude of the step pulse can be adjusted by scanning to generate current pulses with varying charges.

Fig. 11 shows the linearity test results for one of the readout channels for both IDE3380 and VATA160. The VA parts of the VA160 and VATA160 are identical, and their results are similar. According to the test results, the linear range, noise, and equivalent noise charge of the IDE3380 channel are approximately $0 \sim 800\,\mathrm{pC}$, $1\,\mathrm{LSB}$, and $0.21\,\mathrm{pC}$, respectively, whereas the integral nonlinearity of the channel is less than 0.5%. By contrast, the linear range, noise, and equivalent noise charge of the VATA160 channel are approximately $0 \sim 12\,\mathrm{pC}$, $1.2\,\mathrm{LSB}$, and $4.41\,\mathrm{fC}$, whereas its integral nonlinearity is less than 1%.

C. Gain ratio between photodetectors

Fig. 12 shows an experimental device that utilizes a light-emitting diode (LED) to calibrate the relative gain coefficients between each photodetector channel. The LEDs are installed at one end of the BGO crystal, and the signal source generates voltage pulses to drive the LEDs to produce light pulses, which can simulate the light pulses emitted by the BGO crystal. The signal source can generate an approximate exponentially decaying pulse signal through programming or alter-

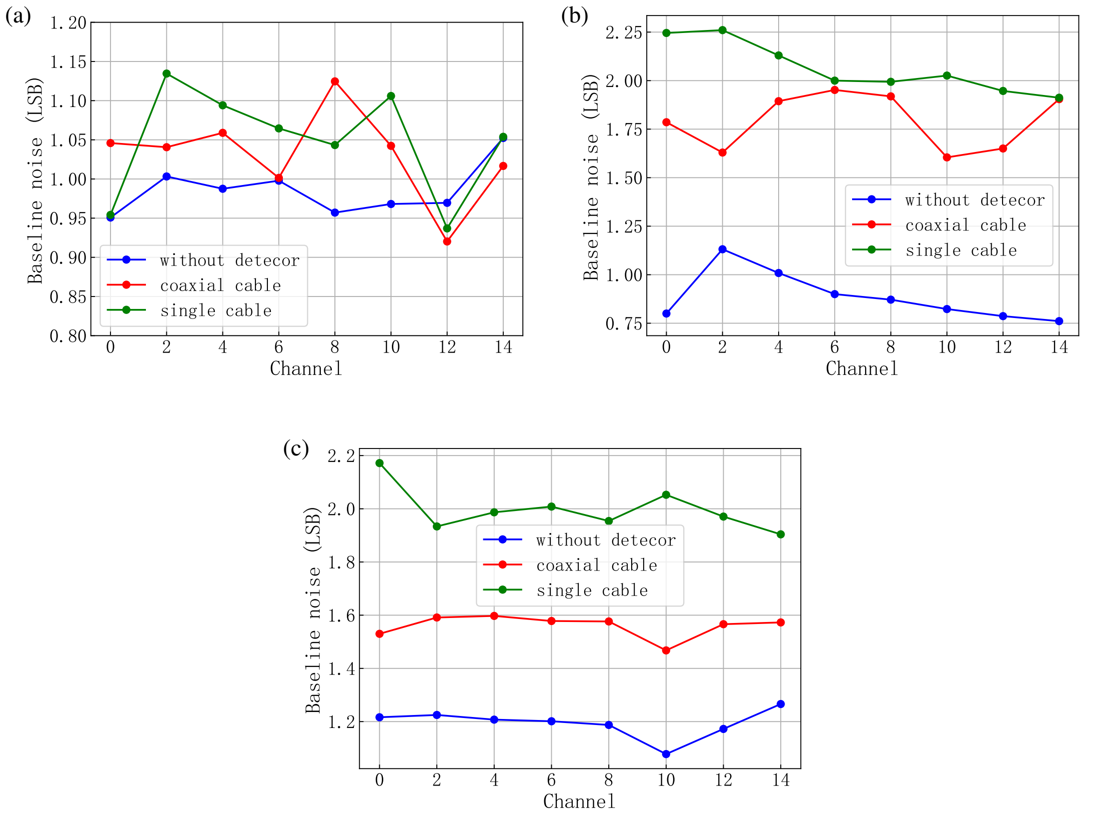

Fig. 10. Test results of the baseline noise. (a) SiPM and IDE3380, (b) L-PD and VATA160, (c) S-PD and VA160.

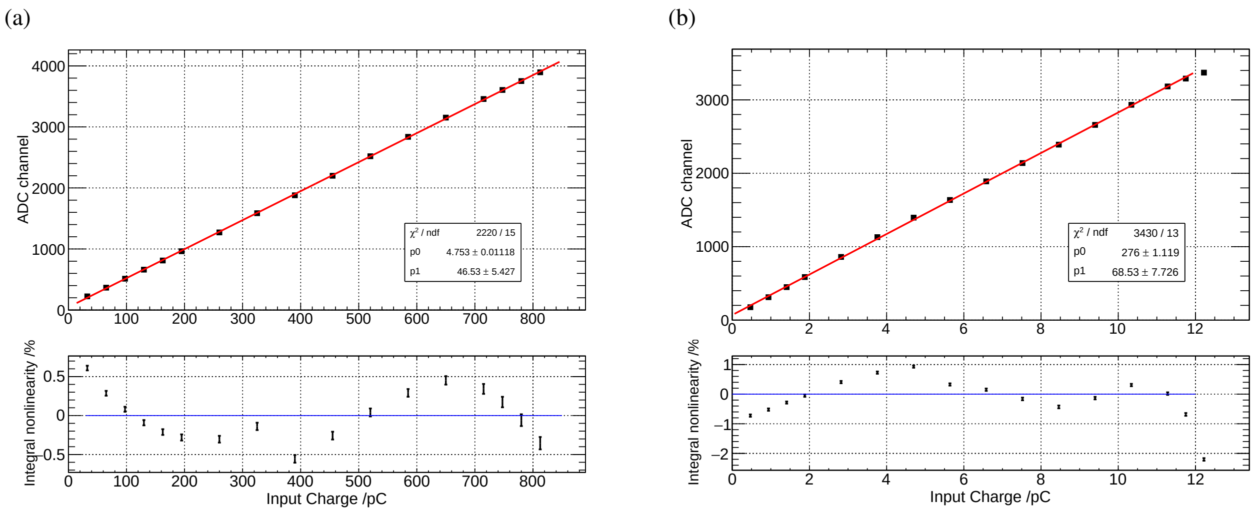

Fig. 11. Test results of electronic linearity. (a) IDE3380, (b) VATA160

natively replace it with a trapezoidal pulse signal. The light signal intensity of the LED can be altered by controlling the amplitude of the pulse signal [30].

At the opposite end of the BGO crystal, a photodetector substrate comprising the SiPM, L-PD, and S-PD was mounted. To distribute the light signals from the LEDs to the detector face as evenly as possible, two layers of Teflon film were attached to each end of the BGO crystal. The relative gain coefficient between each detector and its respective readout channel was obtained by measuring the output at varying optical signal intensities.

The test results are shown in Fig. 13. Linear fitting of the data revealed a gain of 41 times between the SiPM (IDE3380) and L-PD (VATA160) channels and a gain of 23 times be-

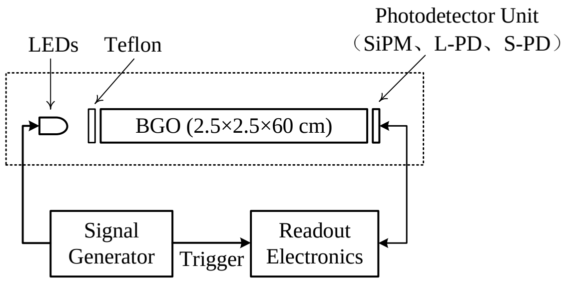

Fig. 12. Block diagram of the device that utilizes LEDs for measuring gain ratio

tween the L-PD (VATA160) and S-PD (VA160) channels. However, the luminescence of the LED is typically limited to a specific emission angle range, which differs significantly from the luminescence of high-energy particles in the scintillator that occurs at all angles. Consequently, the test results from the LED may not accurately reflect the actual situation. Thus, further beam experiments are necessary to obtain more precise results.

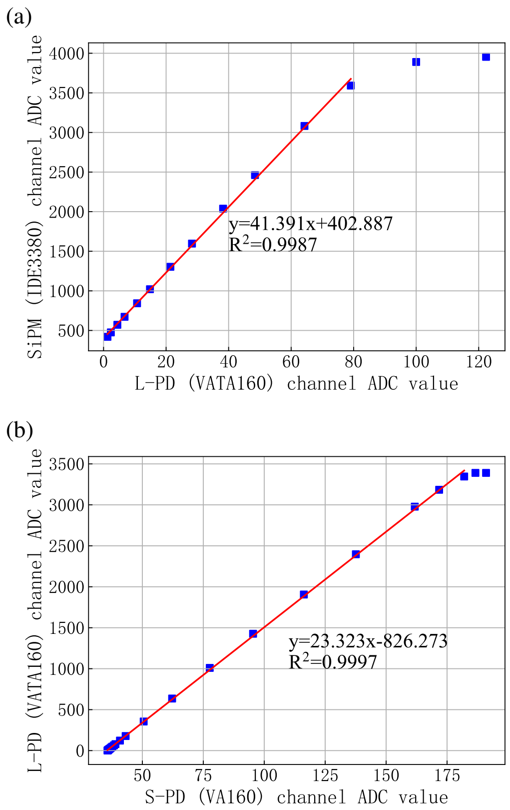

Fig. 13. Test results of the gain ratio between the photodetector. (a) SiPM channel and L-PD channel, (b) L-PD channel and S-PD channel.

D. Ground-based cosmic ray test

Muons in cosmic rays that reach the Earth‘s surface tend to pass through the layers of crystals in the calorimeter in an approximately straight path, and the corresponding response of the detector unit is generally the minimum ionizing particle signal. Testing the prototype system of the calorimeter module using cosmic ray muons can prove the collaborative performance of each module. Fig. 14 shows a schematic of the experimental device for the ground-based cosmic ray measurement of the calorimeter module. A plastic scintillator detector (PSD) was used to generate the trigger signal during the test. The PSD was positioned directly above the overlapping areas of the six layers of crystals in the calorimeter. The signal from the PSD was read by a PMT, and a constant fraction discriminator (CFD) was used to produce the trigger signal, which was connected to the external trigger interface of the electronic system.

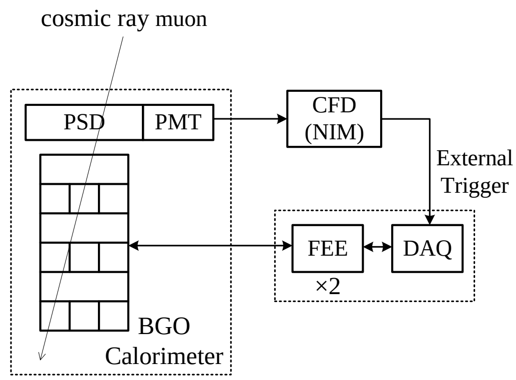

Fig. 14. Block diagram of the test device of the calorimeter module

The cosmic ray experiment was performed for 48 hours. Because the calorimeter must measure a higher range of energies and the energy of the cosmic-ray MIP is relatively small, only the SiPM channel with the highest gain can detect a clear MIP signal. The energy spectra of the cosmic rays measured by all detector units in the calorimeter module were consistent. Fig. 15 shows the MIP energy spectra measured by the SiPM channel in the 1st, 3rd, and 5th layers. The spectra were fitted with a Landau convoluted Gaussian function, and their MPV peaks were approximately 10 ADC values (excluding the baseline). Based on the linearity calibration results for the readout channels, the input charge corresponding to the MIP signal was estimated to be approximately $2.6\,\mathrm{pC}$.

According to the calibration of the absolute energy of the MIP in the cosmic ray experiment and the gain between the photodetectors in the LED experiment, it can be estimated that the noise level of the SiPM channel with the highest gain is approximately $0.1\,\mathrm{MIPs}$, and the upper limit of energy that the SiPM channel can measure exceeds $200\,\mathrm{MIPs}$. The entire crystal detector unit has an upper energy measurement limit close to that of $2 \times 10^5\,\mathrm{MIPs}$, and the dynamic range is as

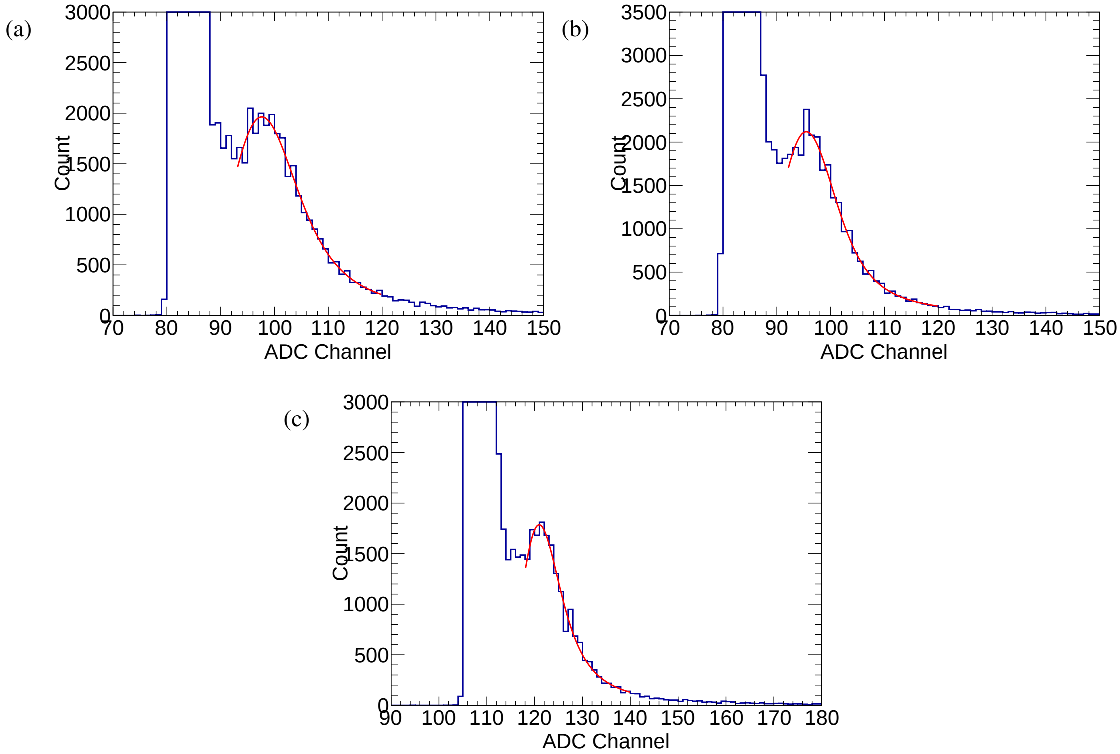

Fig. 15. MIP spectra measured by the SiPM channel. (a) layer 1, (b) layer 3, (c) layer 5.

high as 10^6.

VI. CONCLUSION

This paper presents a high-dynamic-range readout scheme for the VLAST calorimeter and the design of a prototype readout system. Based on the currently selected photodetectors and readout electronics, the dynamic range of a single crystal detector is expected to be close to 10^6. To optimize the dynamic range of the entire readout system, several measures will be implemented to fine-tune the energy range covered by each photodetector in future studies. For example, the optical wrapper of the scintillation crystal can be replaced to enhance the fluorescence collection efficiency of SiPM, thereby enabling the detection of signals with lower energy. Furthermore, optical attenuators will be employed on the S-PD to facilitate the detection of signals with higher energies.

The calorimeter prototype system is also undergoing improvements by optimizing the connection between the detector and the electronics, implementing a dual-end readout for each BGO bar, and planning beam experiments to further verify the readout scheme.

[1] M. Ajello, W. B. Atwood, M. Axelsson et al., Fermi Large Area Telescope Performance after 10 Years of Operation. The Astrophysical Journal Supplement **256**, 12 (2021). doi: 10.3847/1538-4365/ac0ceb

[2] R. Caputo, M. Ajello, C. A. Kierans et al., All-sky Medium Energy Gamma-ray Observatory eXplorer mission concept. Journal of Astronomical Telescopes, Instruments, and Systems **8**, 044003 (2022). doi: 10.1117/1.JATIS.8.4.044003

[3] N. P. Topchiev, A. M. Galper, I. V. Arkhangelskaja et al., Gamma- and Cosmic-Ray observations with the GAMMA-400 Gamma-Ray telescope. Advances in Space Research **70**, 2773-2793 (2022). doi: 10.1016/j.asr.2022.01.036

[4] F. Alemanno, on Behalf of the DAMPE Collaboration, The DAMPE Space Mission: Status and Main Results. Moscow University Physics Bulletin **77**, 280-283 (2022). doi: 10.3103/S0027134922020060

[5] G. Ambrosi, Q. An, R. Asfandiyarov et al., Direct detection of a break in the teraelectronvolt cosmic-ray spectrum of electrons and positrons. Nature **552**, 63-66 (2017). doi: 10.1038/nature24475

[6] Q. An, R. Asfandiyarov, P. Azzarello et al., Measurement of the cosmic ray proton spectrum from 40 GeV to 100 TeV with the DAMPE satellite. Science Advances **5**, aax3793 (2019). doi: 10.1126/sciadv.aax3793

[7] F. Alemanno, Q. An, P. Azzarello et al., Measurement of the Cosmic Ray Helium Energy Spectrum from 70 GeV to 80 TeV with the DAMPE Space Mission. Physical Review Letters **126**, 201102 (2021). doi: 10.1103/PhysRevLett.126.201102

[8] DAMPE Collaboration, Search for gamma-ray spectral lines with the DArk Matter Particle Explorer. Science Bulletin **67**,

679-684 (2022). doi: 10.1016/j.scib.2021.12.015

[9] DAMPE Collaboration, Detection of spectral hardenings in cosmic-ray boron-to-carbon and boron-to-oxygen flux ratios with DAMPE. Science Bulletin **67**, 2162-2166 (2022). doi: 10.1016/j.scib.2022.10.002

[10] F. Gargano, on behalf of the HERD collaboration, The High Energy cosmic-Radiation Detection (HERD) facility on board the Chinese Space Station: hunting for high-energy cosmic rays. Proceedings of Science **ICRC2021**, 026 (2021). doi: 10.22323/1.395.0026

[11] L. Pacini, O. Adriani, Y. l. Bai et al., Design and expected performances of the large acceptance calorimeter for the HERD space mission. Proceedings of Science **ICRC2021**, 066 (2021). doi: 10.22323/1.395.0066

[12] A. De Angelis, M. Mallamaci, Gamma-ray astrophysics. The European Physical Journal Plus **133**, 324 (2018). doi: 10.1140/epjp/i2018-12181-0

[13] S. L. Feng, P. Fan, Y. F. Hu et al., The Review of gamma-ray Astrophysics Observing Techniques. Acta Astronomica Sinica **62**, 6 (2021). doi: 10.15940/j.cnki.0001-5245.2021.01.006

[14] R. Caputo, ICRC 2021: Gamma-ray Direct Rapporteur. Proceedings of Science **ICRC2021**, 045 (2021). doi: 10.22323/1.395.0045

[15] Y. Z. Fang, J. Chang, J. H. Guo et al., Very Large Area Gamma-ray Space Telescope (VLAST). Acta Astronomica Sinica **63**, 27 (2022). doi: 10.15940/j.cnki.0001-5245.2022.03.002

[16] H. B. Yang, X. Q. Li, Y. H. Yu et al., Design and evaluation of prototype readout electronics for nuclide detector in Very Large Area Space Telescope. Nuclear Science and Techniques **33**, 65 (2022). doi: 10.1007/s41365-022-01047-5

[17] J. J. Wei, J. H. Guo, Y. M. Hu, Characterization of silicon microstrip sensors for space astronomy. Nuclear Science and Techniques **31**, 97 (2020). doi: 10.1007/s41365-020-00811-9

[18] J. Chang, G. Ambrosi, Q. An et al., The DArk Matter Particle Explorer mission. Astroparticle Physics **95**, 6-24 (2017). doi: 10.1016/j.astropartphys.2017.08.005

[19] S. Alnussirat, C. Altomare, R.G. Bose et al., The Advanced Particle-astrophysics Telescope: Simulation of the Instrument Performance for Gamma-Ray Detection. Proceedings of Science **ICRC2021**, 590 (2021). doi: 10.22323/1.395.0590

[20] J. E. Grove, W. N Johnson, on behalf of the Fermi LAT Collaboration, The calorimeter of the Fermi Large Area Telescope. Proceedings of SPIE **7732**, 77320J (2010). doi: 10.15940/10.1117/12.857839

[21] O. Adriani, Y. Akaike, K Asano et al., The CALorimetric Electron Telescope (CALET) for high-energy astroparticle physics on the International Space Station. Journal of Physics: Conference Series **632**, 012023 (2015). doi: 10.1088/1742-6596/632/1/012023

[22] O. Adriani, M. Antonelli, A. Basti et al., Development of the photo-diode subsystem for the HERD calorimeter double-readout. Journal of Instrumentation **17**, P09002 (2022). doi: 10.1088/1748-0221/17/09/P09002

[23] C. Q. Feng, D. L. Zhang, J. B. Zhang et al., Design of the Readout Electronics for the BGO Calorimeter of DAMPE Mission. IEEE Transactions on Nuclear Science **62**, 3117-3125 (2016). doi: 10.1109/TNS.2015.2479091

[24] Y. F. Wei, Z. Y. Zhang, Y. L. Zhang et al., Performance of the BGO Detector Element of the DAMPE Calorimeter. IEEE Transactions on Nuclear Science **63**, 548-551 (2016). doi:10.1109/TNS.2016.2541690

[25] C. Zhao, H. T. Dai, C. M. Liu et al., The study of fluorescence response to energy deposition in the BGO calorimeter of DAMPE. Nuclear Instruments and Methods in Physics Research Section A: Accelerators, Spectrometers, Detectors and Associated Equipment **1092**, 166453 (2022). doi: 10.1016/j.nima.2022.166453

[26] Integrated Detector Electronics AS Inc., Integrated Circuits Products - IDEAS. https://ideas.no/ideas-ic-products/

[27] Y. Zhang, J. H. Guo, Z. Zhang et al., Spectrometer of hard X-ray imager payload onboard the ASO-S mission. Nuclear Science and Techniques **30**, 128 (2019). doi: 10.1007/s41365-019-0642-y

[28] Q. Wan, J. H. Guo, Y. Zhang et al., Radiation tolerance of the charge measurement ASIC for the ASO-S HXI spectrometer. Nuclear Techniques **46**, 030203 (2023). doi: 10.11889/j.0253-3219.2023.hjs.46.030203

[29] Y. Q. Zhang, J. H. Guo, L. Yang et al., Design and on-orbit status of the trigger system for the DAMPE mission. Research in Astronomy and Astrophysics **19**, 123 (2019). doi: 10.1088/1674-4527/19/9/123

[30] T. Xiang, X. Jin, J. N. Dong et al., Study of linearity for a high dynamic range calorimeter. Chinese Physics C **38**, 046201 (2014). doi: 10.1088/1674-1137/38/4/046201